Structural and magnetic characterization of (FeCo)$_{1-x}$Cr$_x$ nanowires array prepared by pulsed electrodeposition

Ebrahim Paimozd[1] · Omid Mirzaee[1] · Ali Ghasemi[2] · Mohammad Tajally[1]

Abstract

(FeCo)$_{1-x}$Cr$_x$ nanowires (NWs) were grown by a pulsed AC electrodeposition technique into aluminum oxide nanoporous templates with good consistency. The structural features and morphologies of the NWs array were examined by X-ray diffraction (XRD) and field emission scanning electron microscopy (FESEM). A vibrating sample magnetometer equipped with the first-order reversal curve (FORC) diagram was then used to find the magnetic properties. The formation of NW with the (110) texture was also confirmed for the whole series samples. With increasing the Cr addition on the FeCo NW arrays, the corresponding diffraction peak in the XRD patterns was shifted to the lower angles and the lattice constant was increased. FE-SEM analysis also revealed that (FeCo)$_{1-x}$Cr$_x$ NWs with the length of 10 μm were grown above the Cu pre-plating layer into aluminum oxide with the pore diameter of 30 nm. Further, the hysteresis loops showed that the coercivity were decreased from 2265 to 1388 Oe, respectively, with an increase in the Cr content from the concentration of 0 to 0.03 M. FORC diagrams proved a decrease of the magnetostatic interaction with Cr content and a non-interacting single domain structure for the maximum Cr addition. Local magnetic interactions were also found to prevail in the presence of the Cr element beside the magnetic phase.

Keywords FeCo nanowires · Magnetic properties · FORC diagrams · Electro-deposition

1 Introduction

The magnetic NWs are appropriate potential candidates for application in nanotechnology, spintronics, microwave devices [1], recording media [2], biotechnology or biomedicine [3], and giant magnetoresistance sensors (GMR) [4–6]. Magnetic features of NWs are dominantly controlled by the competition of shape anisotropy, inter-wire magnetostatic interaction and magnetocrystalline anisotropy. The variation of such anisotropies is based on effective parameters including the dimension, composition and annealing of NWs [7–9].

NWs have been fabricated with different methods such as chemical vapour deposition [10], lithography [11], sol–gel synthesis [12], and electrodeposition process [13]. The AC pulsed electrodeposition could serve as a reliable method to produce a uniform nanowire growth within the anodized aluminum oxide template [14–16].

FeCo binary alloys with a bcc structure are a soft magnetic phase material with high saturation magnetization, low coercivity and a high Curie temperature. The tendency for the development of the high coercivity system based on 3d transition metals is a novel approach. For this purpose, FeCo with a prolate spheroid feature including NW was fabricated with high saturation magnetization and large shape anisotropy and the very large coercivity of 10 kOe [8]. The value of coercivity in the single domain NWs array was almost three times smaller than the anisotropy field correlated to the magnetostatic interaction between wires. The nature of magnetostatic interaction is strongly influenced by the volume fraction of the ferromagnet in the template [17, 18].

Electrodeposition conditions including current density, deposition frequency, pH value and temperature of the electrolyte could influence the structural characteristics of NWs.

✉ Ebrahim Paimozd
paimozd@gmail.com

✉ Omid Mirzaee
o_mirzaee@semnan.ac.ir

1   Faculty of Materials and Metallurgical Engineering, Semnan University, Semnan, Iran

2   Materials Engineering Department, Malek Ashtar University of Technology, Shahin Shahr, Iran

A preferential growth along the easy axis could be achieved by modifying these parameters that could enhance the magnetic properties of FeCo NWs. The variation in the reductive-oxidative voltage increases the growth rate of NWs and coercivity [19]. However, the saturation magnetization of FeCo is independent of the sample morphology; the high aspect ratio NWs have higher coercivity in comparison to the other morphologies due to shape anisotropy [20]. The effect of shape anisotropy is the same for NWs with an aspect ratio higher than 10. On the other hand, the magnetic properties can be tuned through changing geometrical features such as NWs diameter, inter-wire distance, length, and diameter modulation. In this regard, a decrease in the NWs diameter increases the coercivity, which can be related to the magnetostatic interaction between the NWs and the transition between reversal modes [21].

Incorporation of a tiny amount of non-magnetic elements could be very influential on the magnetic behavior of the NW arrays. The additional elements such as copper [22–25], boron [26], lead [27] and nickel [28, 29] were added to FeCo NWs to change the microstructure and magnetically characterize the synthesized NWs. Magnetic and structural properties of CoFe and CoFeB NWs were also investigated by Sharif and colleagues [26]. They found that the amorphous phase of $Co_{94}Fe_6$ and $Co_{91}Fe_6B_3$ was obtained. They also recognized that induced magnetic anisotropy with preferred crystalline orientations was achieved by magnetic field annealing and re-annealing at 600 °C. In one other research, the magnetic properties of CoFe with Cu addition were fully evaluated using the FORC analysis [30]. It was found that a hard magnetic phase was formed by annealing NWs. The high level of the Cu substitution led to the appearance of the soft phase. Bran and colleagues demonstrated that adding the Cu atoms to FeCo enhanced the process of magnetic hardening [31]. Maximum coercivity of 4700 Oe and squareness of 0.98, as measured at 10 k, were obtained for FeCoCu NWs with the diameter of 18 nm by annealing at 500 °C. Thermal annealing of FeCoCu and the effect of the Cu addition to FeCo NWs array have also been studied, indicating that magnetic hardening could be promoted by annealing [23, 32]. Therefore, the improvement of shape anisotropy through the high aspect ratio [20], the control of composition [33], the use of multi-step [34] and asymmetric [19] electrodeposition voltage for the microstructure modification, the substitution of different elements [22–29], and thermal annealing [23, 32, 33] have been considered to tune and reinforce the magnetic properties of FeCo NWs.

Previous studies have shown that by adding magnetic or non-magnetic elements to FeCo NWs, the structural and magnetic properties of single crystals are turned and the nature of matter could be tailored [23, 31, 32]. To the best of our knowledge, there is no prior work regarding on FeCoCr NWs.

Therefore, in the present work, the AAO templates were successfully prepared using two-step anodizing. Then, $(FeCo)_{1−x}Cr_x$ NWs with various chromium concentrations were grown into templates. Subsequently, the magnetic analyses were carried out by the hysteresis curves and FORC diagrams were obtained for all of the samples. XRD patterns also confirmed the magnetic behavior of the NW arrays. These results indicated the structural dependence of the magnetic properties of $(FeCo)_{1−x}Cr_x$ NWs. The correlation between structural features and magnetic analyses was investigated and the coercivity mechanism was interpreted by FORC analyses.

2 Materials and methods

The AAO template was synthesized using the 99.997% pure aluminum disk as the precursor, as provided from Alfa Aesar. Starting materials were first ultrasonically washed and then electropolishing was carried out into a solution of ethanol and perchloric acid (1:4 in volume) with a current density of 100 mAcm^{-2}. The first step was anodizing, which was performed using 0.3 M oxalic acid for 6 h under the constant potential of 40 V at 17 °C. The oxide layer was then etched in 0.2 M chromic acid and 0.5 M phosphoric acid. The second step of anodization was carried out under the same conditions, as done for the first step, for 2 h. To reach the suitable barrier layer, the thinning second step of the anodizing potential was reduced to 10 V with a decreasing rate of 0.001 V/sec.

To synthesize $(FeCo)_{1-x}Cr_x$ NWs array inside the alumina template, an electrolyte including 0.15 M $FeSO_4.7H_2O$, 0.15 M $CoSO_4.7H_2O$, 0.7 M H_3BO_4 and 0.005 M ascorbic acid was prepared. Then, $Cr_2(SO_4)_3$ with the concentrations of 0.001–0.03 M was also added to the electrolyte solution, according to Table 1.

The key effective parameters employed in the current research to get highly sufficient NWs are listed in Table 2. The deposition was performed at 30 °C and the acidity of the solution was kept constant at 3 using $NaHCO_3$. To obtain uniform NWs during electrodeposition, Cu pre-plating was used to fill the branched pores. Electrodeposition was performed in a 0.3 M $CuSO_4.7H_2O$ electrolyte. The temperature of the barrier layer was adjusted at 8 °C. The barrier layer served an

Table 1 Identification of NW arrays according to the molar concentrations of chromium

	0	0.001	0.002	0.003	0.006	0.01	0.03
Sample number	Cr-0	Cr-1	Cr-2	Cr-3	Cr-6	Cr-10	Cr-30

Table 2 Electrodeposition conditions for (FeCo)$_{(1-x)}$Cr$_x$ NW and Cu pre-plating

Composition	Reduction/oxidation voltage (V)	Pulse time (ms)	Off-time (ms)	Current density (mAcm^{-2})	Deposition charge (C)
(FeCo)$_{(1-x)}$Cr$_x$	12/11	2.5	50	50	1
Cu	12/11	2.5	50	60	0.1

important role in current rectification as electrons were provided for cathodic reactions.

Finally, the samples were mounted and the aluminum substrate was dissolved by immersing it in a solution of CuCl$_2$. The crystalline structure of NWs was studied based on the XRD analysis, using Philips X'Pert Pro; this was done using Cu $k\alpha$ radiation, $\lambda = 0.145$ nm, which was run at a voltage at 40 kV and 30 mA (with the step size of 0.05 and the time per step of 0.5 s). To eliminate alumina and identify NWs for the morphological investigation, the samples were etched in a solution of NaOH at the room temperature. Field emission scanning electron microscope (FESEM-MIRA3SCAN) equipped with energy dispersed X-ray spectrometer (EDS) analysis operating at 15 kV was employed. FE-SEM was also conducted to investigate the morphology and identify the dimensions of the NWs arrays. The hysteresis loop and angular dependence of magnetization were measured at the room temperature by applying the vibrating sample magnetometer. To thoroughly interpret the magnetic interaction and the trend of magnetic domains, first-order reversal curve analysis was recorded. To follow this approach, the specimen was first saturated to H_S and this was followed by the reduction to reversal field (H_r). Then, the magnetic field was increased in the minus direction to reach the saturation field and the saturation value M (H,Hr) was measured in each single step. This procedure was repeated by considering the boundary condition of Hr $\geq -$ Hs. The details of the procedure could be found in the literature [35–37]. The distribution of FORC is defined by:

$$\rho(H, H_r) = -\frac{1}{2}\frac{\partial^2 M(H, H_r)}{\partial H \partial H_r} \tag{1}$$

To obtain a counter plot of the FORC diagram, the coercive field (H_c) and interaction field (H_u) axes are expressed by [35–37]:

$$H_c = \frac{H - H_r}{2}, H_u = \frac{H + H_r}{2} \tag{2}$$

3 Results and discussion

3.1 Electrochemical consideration

Figure 1 represents the time dependence of the potential during the electro-deposition process for whole series of Cr

concentrations. To stabilize the deposition current density at 50 mAcm^{-2}, the deposition potential was varied from 11 to a maximum value of 16.3 V for Cr-0. With an increase in the Cr content, the final voltage was declined, reaching the minimum of about 14 V for the high level of the Cr substitution in the last stage of the process.

The molar concentration of metal ions had a considerable influence on the electro-deposition current density. To reach the uniform filling of the pores, the current density was kept at the stable value of 50 mAcm^{-2}. It was found that the addition of Cr could meet the requirement at the lower applied potential.

It was revealed that with increasing the Cr content, the corresponding potential was as $E_{Cr-0} > E_{Cr-2} > E_{Cr-1} > E_{Cr-3} > E_{Cr-6} > E_{Cr-30} > E_{Cr-10}$. The potential for the samples Cr-10 and Cr-30 had an ascending trend without any stabilization up to 5000 s. The variation of potential could be interpreted by the ohm's law. It should be noted that the impedance could originate from the electrolyte solution resistance, the barrier layer solution interface or the impedance of the nonporous alumina membrane, and the dielectric constant of the oxide barrier layer [38]. In the current research, as the resistivity of the barrier layer remained constant, the voltage value was remarkably affected by the solution resistance and the solution ions
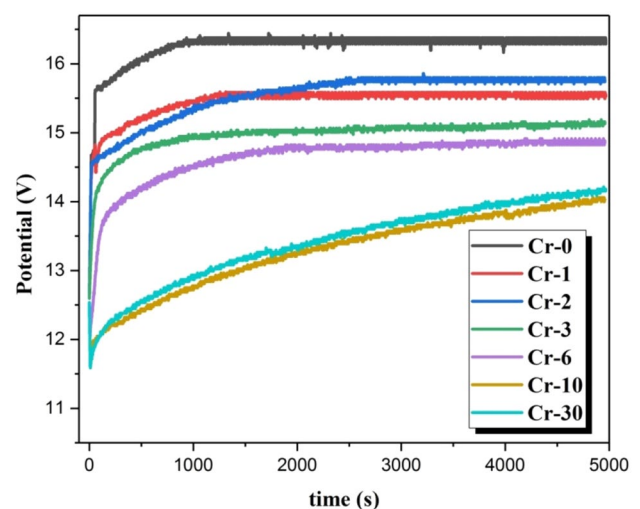

Fig. 1 Deposition profiles recorded for different Cr concentrations during electrodeposition to reach the current density of 50 mAmcm^{-2} at 30 °C

conductivity determined the required potential to reach the current constant.

Although mechanical stirring could help metal ions to move in solution, due to the limited diffusion, as previously reported [13, 39], ions are transported inside the pores controlled by the diffusion; this can be expressed by the Fick's law. The current density of electro-deposition is followed by the number of charges, the diffusion coefficient of the electroactive spies, the bulk concentration of this species and the diffusion layer [39]. Hence, the diffusion coefficient and concentration of Cr ions were influential in determining the value of current density and reaching different potential levels.

In this work, the deposition temperature was kept constant at 30 °C, leading to the uniform growth of NWs. Higher temperature forced the iron ions to be oxidized and H_2 bubbles formation made an obstacle for the deposition of metals.

3.2 Structural and morphological study

XRD patterns of the NWs embedded into AAO templates with different Cr concentrations are presented in Fig. 2a. The Cr-0 sample with the BCC structure was grown along the $<110>$ direction. Based on the previous works, the high intensity diffracted peak was at $2\theta = 44.7°$, confirming the formation of FeCo [40, 41]. The peak intensity of (110) was increased from Cr-0 to Cr-3; it was decreased with increasing the Cr content. The alumina template could appear according to background in the XRD patterns. The Cr phase also appeared for the samples Cr-10 and Cr-30 with a higher concentration.

With an increase in the Cr concentration, the (110) peak was slightly shifted to the lower angles, as shown in Fig. 2b. Cr atoms were dissolved in the FeCo structure and the shift was a sequence of the variation of d-spacing and the lattice constant. The lattice constant was calculated using the Bragg's law and the equation $d = \frac{a}{\sqrt{h^2+k^2+l^2}}$ (d is the interplanar spacing, a is the lattice constant, and h, k, and l are the values of the Miller indices of the diffraction peak) according to the results obtained for the (110) diffraction peak, as shown in Fig. 2c. The trend was well consistent with the previous report [40].

Figure 2d shows the atomic percentage of Cr in the nanowires with Cr percentage in electrolyte and EDS spectra. A typical cross-section view of NWs is also shown in Fig. 3a, displaying that alumina was dissolved and NWs with the length 10 μm were accumulated. Figure 3b shows the top-view micrograph of the porous alumina template. The pores had the average diameter of 30 nm and the inter-pore distance of 100 nm.

The branched dendrite at the bottom of pores was formed by exponentially reducing the anodization voltage at the last step of the anodization process. This dendrite structure was filled by copper using an electro-deposition stage (Fig. 3c). This Cu pre-plating would have resulted in the enhancement of electro-deposition conditions, providing the magnetic properties.

3.3 Magnetic measurement

The magnetic properties of the $(FeCo)_{(1-x)}Cr_x$ NW arrays in the perpendicular direction and at room temperature are presented in Fig. 4a. By adding non-magnetic Cr cations, M_S was reduced from 37 to 17 memu.

The perpendicular coercivities of the whole series of specimens were lower than those for the in-plane measurements. It was found that with an increase in the Cr substitutions, the coercivity and squareness were reduced. Consequently, the magnetic easy axis was along the NW direction. The branched structures filled by copper played an import role in the enhancement of coercivity and squareness for the whole series of the samples.

The variations of coercivity, squareness and saturation magnetization of the NW arrays with the Cr concentration are shown in Fig. 4b. The coercivity was decreased from 2265 Oe for Cr-0 to 1388 Oe for the sample Cr-30. At the low level of the Cr substitution, the lattice parameter was increased, causing the alternation of the magnetocrystalline anisotropy constant, magnetostatic interaction and the exchange of energy. However, for Cr-10 and Cr-30, the existence of the non-magnetic Cr-base phase was proved by XRD; consequently, the saturation magnetization was declined. Similar variations in coercivity were observed by the addition of the diluted value of copper in iron cobalt Nws, as shown in the literature [41].

Magnetization reversal mechanism of NWs was determined by the angular dependence of coercivity, as shown in Fig. 5. It should be noted that, the coercivity values were normalized by the coercivity value at $\theta = 0°$. It was found that the variation reflected the smooth reduction up to $\theta = 45°$ and further increase in the field orientation caused a sharp decrease in trend.

The non-monotonic behavior of H_C in the large applied angles for the FeCo NWs array was comparable with a magnetization reversal model and could be attributed to the nucleation and movement of the domain walls [42–44].This state was preserved in the presence of Cr up to 0.01 M on the sample Cr-10. The diameter of NWs was sufficiently large to create the new domain wall. Bajales [45] also reported the mechanism of nucleation and propagation of a transverse domain wall along the FeCo NWs length, based on the analytic calculation for the transverse domain wall (TDW) [46, 47].
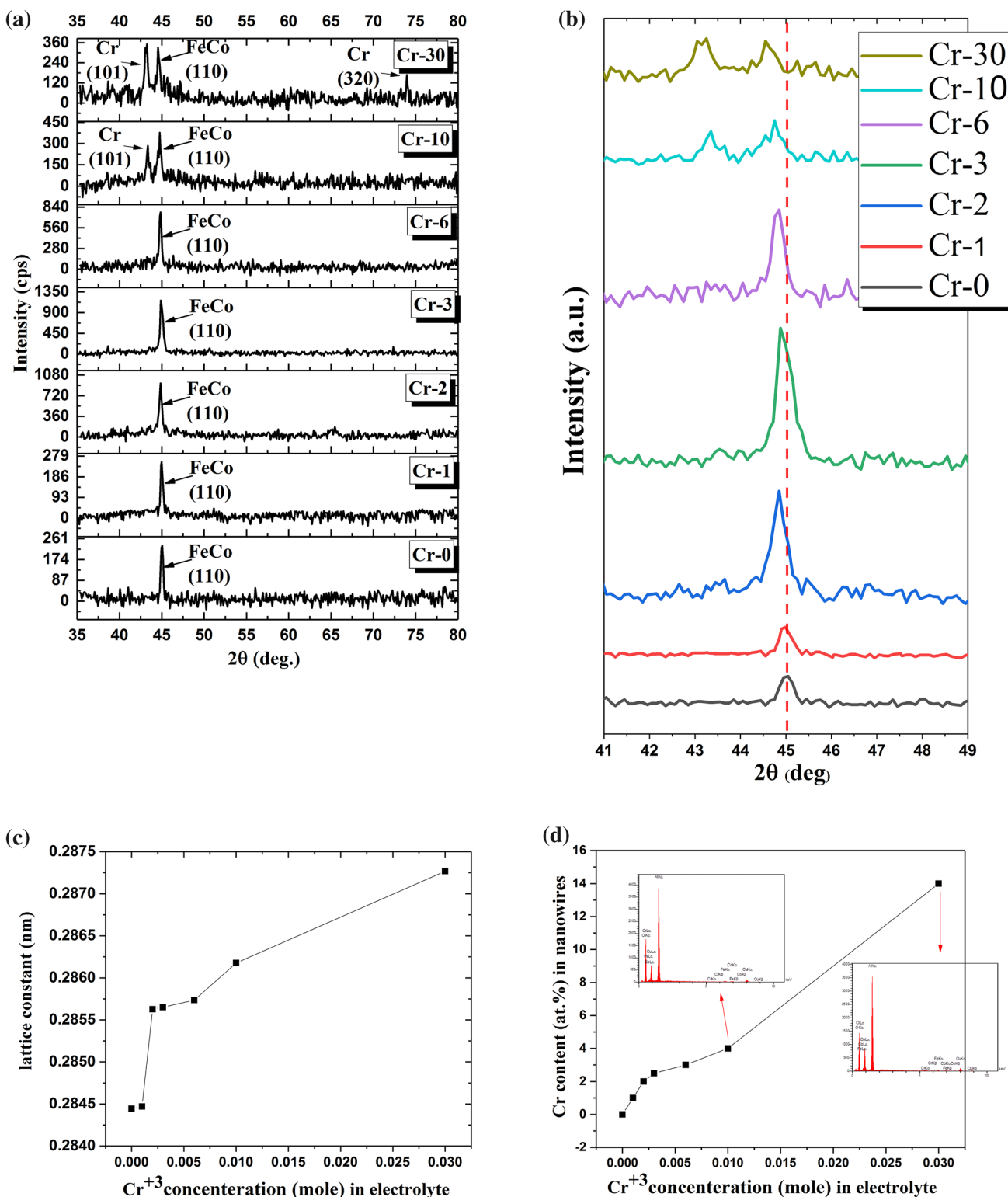
Fig. 2 **a** XRD patterns of the NW arrays, and (**b**) the patterns at (**a**) were re-plotted at 41- 49° for better phase identification. **c** Variation of the lattice constant with Cr^{+3} concentrations (mole) in electrolyte and (**d**) the Cr content in nanowires as a function of Cr^{+3} in the electrolyte and the typical EDS spectra

Fig. 3 **a** Cross-sectional
FESEM image of the NWs of
the sample Cr-2, (**b**) a typical
top view of the FESEM micro-
graph of the alumina template,
and (**c**) the branched dendrite of
Cu at the bottom of the enlarged
micrograph of NWs
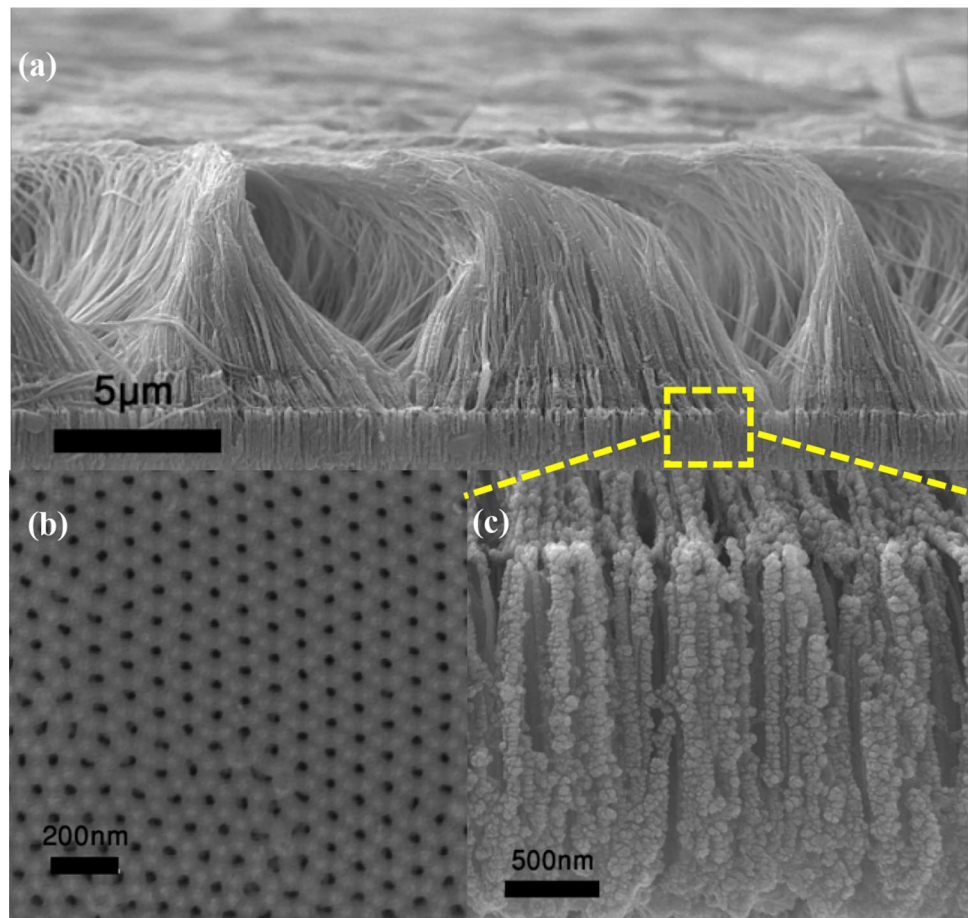
As it is clear, for the sample Cr-30, a decreasing slope
was consistent with the increase of the angle up to 90°, while
for other samples coercivity was sharply reduced at an angle
higher than 60°.

Figure 6 shows chromium dependence of FORC diagrams
as measured in the perpendicular direction of the NW arrays.
This measurement could provide the distribution of the inter-
action and coercive field. FORC diagrams also, indicated the
presence of a single domain phase for the samples. FORC
analyses further confirmed the wide distribution in the FeCo
NWs length that appeared as a narrow tail along the Hc axis.
Based on the analytical and experimental methods, Dobrota
and Stancu demonstrated that the non-uniform length distri-
bution of NWs caused a wide distribution along the Hc axis
[48]. FORC diagrams for the FeCo nanowires also displayed
that the tail was extended more than 4000 Oe, and it was
changed with an increase in the Cr content.

Figure 7c show the variations of H_C^{FORC} and H_C^{array} with
the Cr content. H_C^{FORC} is defined by the peak of the coer-
cive field distribution of the NWs array (Fig. 7b) and H_C^{array}
refers to the coercivity values from the hysteresis loops.

It was clear that with the addition of 0.002 M Cr, H_C^{array}
was decreased from 2265 to 2130 Oe, while H_C^{FORC} was

kept almost constant at 2056 Oe. Comparison of the FORC
distribution width in the H_u direction (Fig. 7b) indicated
an increase in the interaction, resulting in a decrease of the
coercive field of the array.

H_C^{array} and H_C^{FORC} were sharply decreased with increas-
ing the Cr content from 0.002 to 0.01 M concentration. The
variation could be attributed to the magnetic de-coupling of
FeCo containing Cr along the NW length. The magnetostatic
interactions as intra-wire interactions could be reduced due
to the enhanced Cr.

Extension along the H_u axis reflected the existence of the
magnetostatic interaction for FeCo NWs (Fig. 7b). The wide
range distribution with the FWHM of ~ 1500 Oe for Cr-0
is related to the magnetostatic interaction between NWs. It
has been previously reported that for the NWs array with
the length of 3 μm and diameter of 30 nm, FWHM is 2000
Oe [50].

The wide distribution along the H_u direction and the
closed counter centered at the switching field for FeCo
indicated the single domain behavior with the magnetostatic
interaction between the NWs. As can be seen, increasing the
Cr content led to a decrease in the spreading of distribution
along the H_u axis and a decrease for the maximum peak

Fig. 4 a Hysteresis loops of (FeCo)$_{1-x}$Cr$_x$ NWs with different Cr contents. **b** Variation of coercivity, squareness and saturation magnetization of (FeCo)$_{(1-x)}$Cr$_x$ NWs as a function Cr^{+3} concentrations in the electrolyte
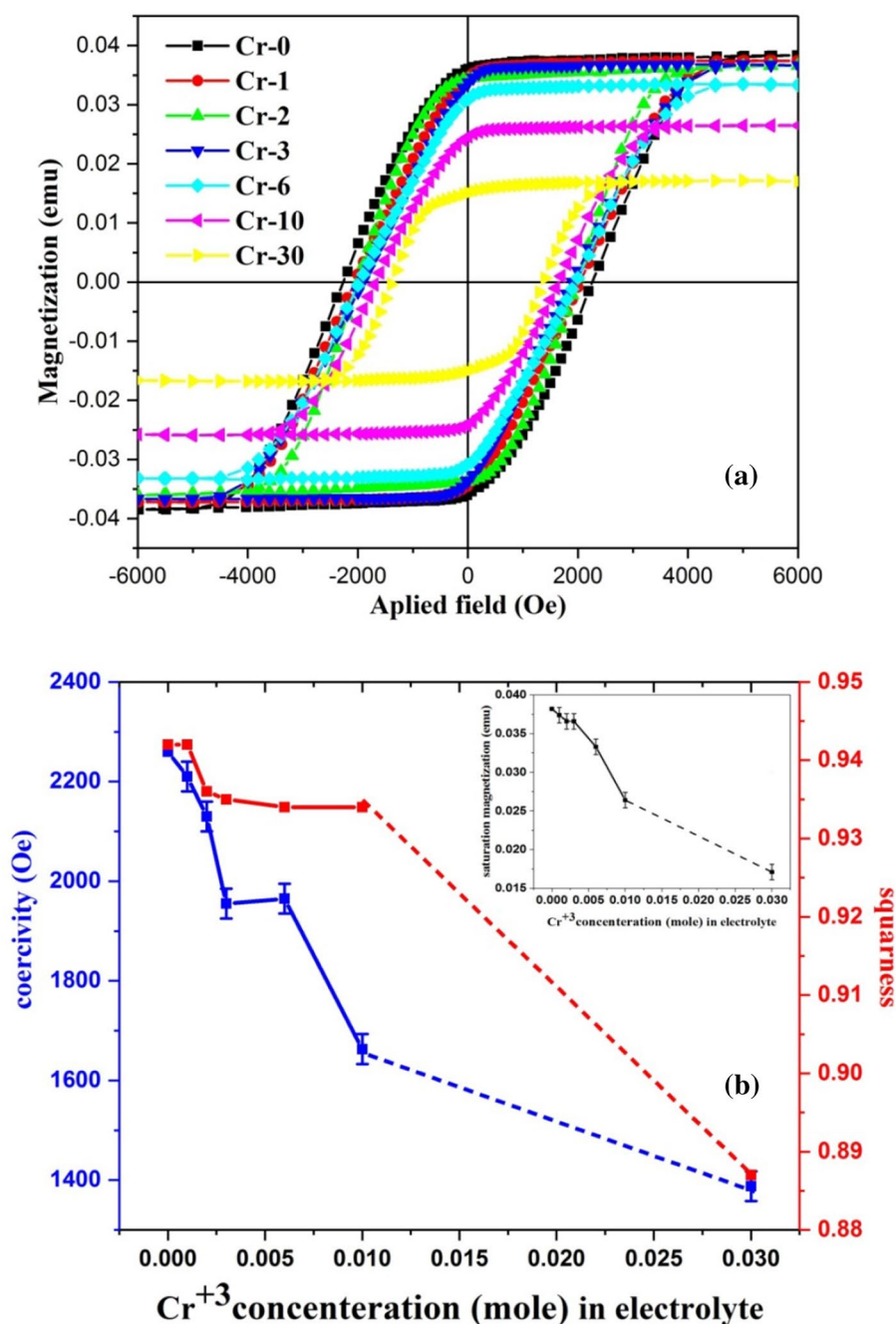
along the H_C axis. At the higher level of the Cr content, the non-magnetic element can be reduced the magnetostatic interactions. Consequently, the non-interacting single domain behavior was dominant for the 0.03 M concentration of Cr.

It is assumed from the moving Preisach model that the interaction between individual magnetic elements at the saturation state follows the relationship [51]:

$$H_{int}^s = 2\sigma_{int} - k, \tag{1}$$

where σ_{int} is the standard deviation of the distribution due to the local interaction and k denotes the mean interaction field in the saturation state. Simulation results have indicated that for the large values $|k|/\sigma_{int}$, the distribution along the H_u axis is widening and the mean magnetostatic interactions between NWs prevail. When the local magnetostatic interactions between magnetic segments are dominant, the peak of plot is sharply ($\sigma_{int} \gg |k|$). The FORC diagram for the
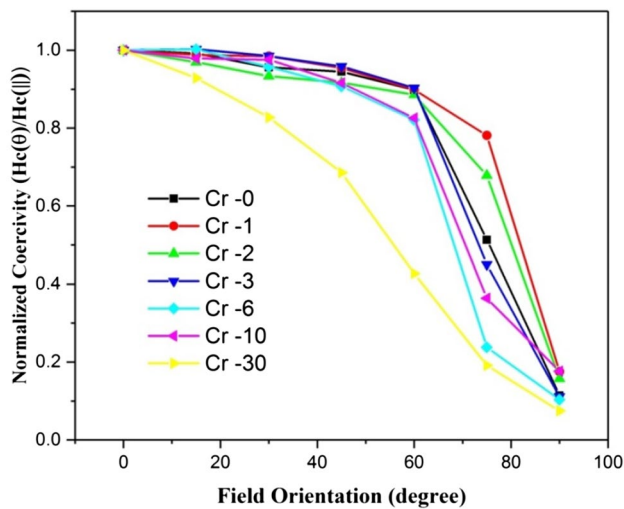
Fig. 5 The angular dependence of coercivity for $(FeCo)_{(1-x)}Cr_x$ NWs

high aspect ratio FeCo NWs array indicates an elongation along the H_u axis which is related to an antiparallel field of the inter-wire interaction [52].

A narrow distribution along the H_u axis and a decrease of the FWHM value appeared for Cr-10 and Cr-30. The presence of the dominant local interaction provides a sharp peak along the H_u axis (Fig. 7a). As confirmed by the XRD analysis, Cr related peak appeared at a higher concentration that might be substituted among the magnetic entities. Consequently, the local magnetic interactions were present in the presence of the Cr element beside the magnetic phase. Figure 8 shows the schematic of inter-wire and intra-wire interactions in the NW arrays.

Additionally, ΔH_u^{FORC} is equal to the inter-wire magnetostatic field at saturation (H_S^{int}) that could be correlated with the saturation magnetization and geometrical feature of NWs such as radius, length, and inter-wire distance [40, 49]. Since the dimension configuration is similar for the whole NWs seen, an increase in the non-magnetic Cr could cause a decrease in the saturation of magnetization and ΔH_u^{FORC}.

4 Conclusion

In this work, $(FeCo)_{1-x}Cr_x$ NWs with a uniform diameter and length were fabricated using the AC pulsed electrodeposition technique in the anodic aluminum oxide template. The Cr addition increases the lattice constant of FeCo in low Cr content and it makes to appear the Cr phase in high Cr content. The increment of the Cr addition to the FeCo NWs array caused a decrease in the saturation magnetization, squareness and coercivity. Experimental results extracted from the angular dependence of coercivity suggested that the magnetization transverse domain wall mode was the dominant mechanism. The FORC diagrams further confirmed the local magnetic interactions occurring in the NWs array for the high Cr content. The FORC diagrams also showed an almost symmetrical wide distribution along the H_C axis with closed contours centered with the dominant interacting single domain for the FeCo NWs array. It was also found that the mean coercivity of the individual NWs was not differently varied by the low addition of Cr. The low Cr addition to FeCo NWs, also made no significant variation in M_S.
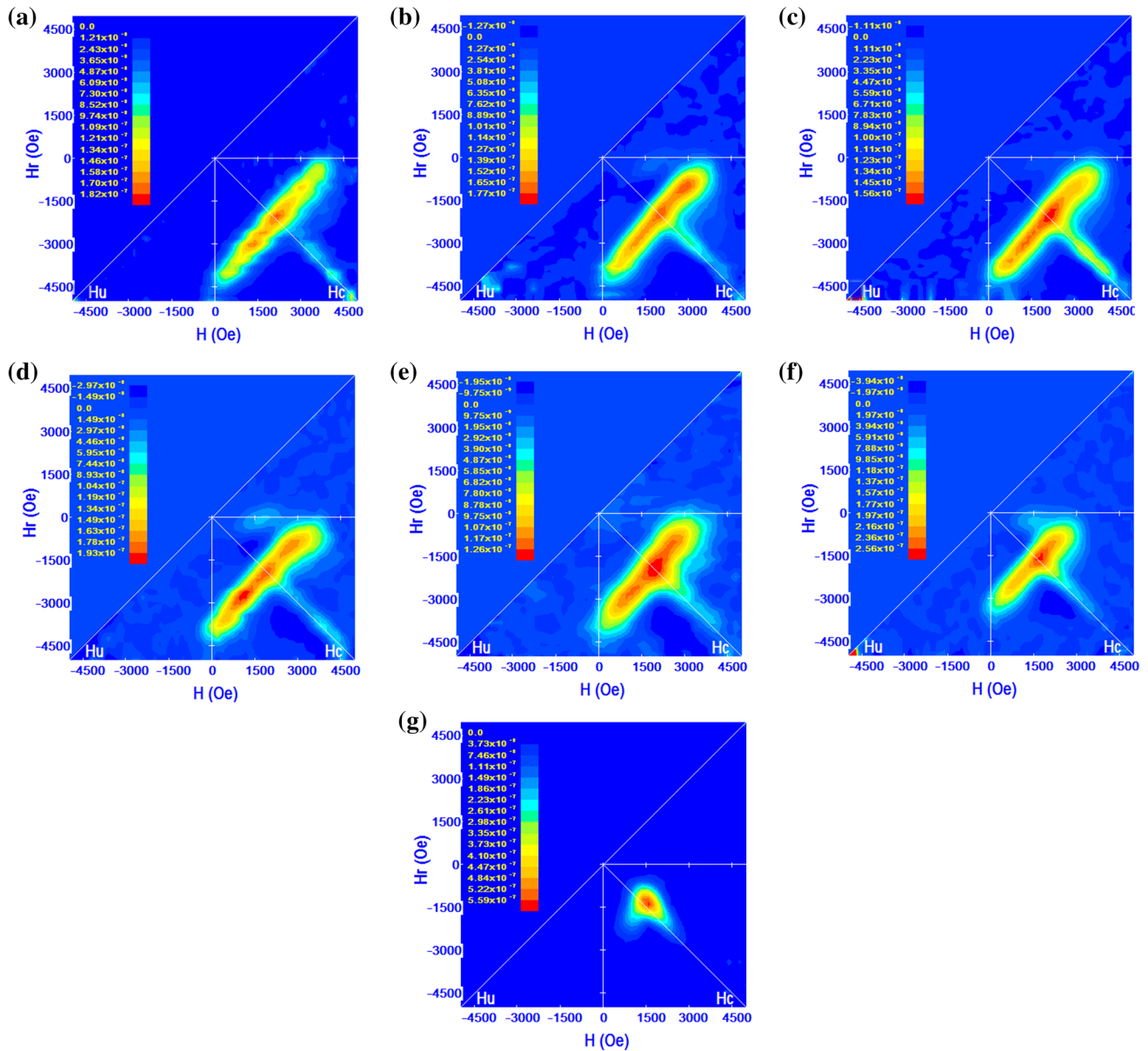
Fig. 6 Out-of-plane FORC diagrams of (FeCo)$_{1-x}$Cr$_x$ NWs for the samples: (**a**) Cr-0, (**b**) Cr-1, (**c**) Cr-2 (**d**) Cr-3 (**e**) Cr-6, (**f**) Cr-10 and (**g**) Cr-30

(a) Interaction Field Distribution (Oe)

(b) Coercive field distribution (Oe)
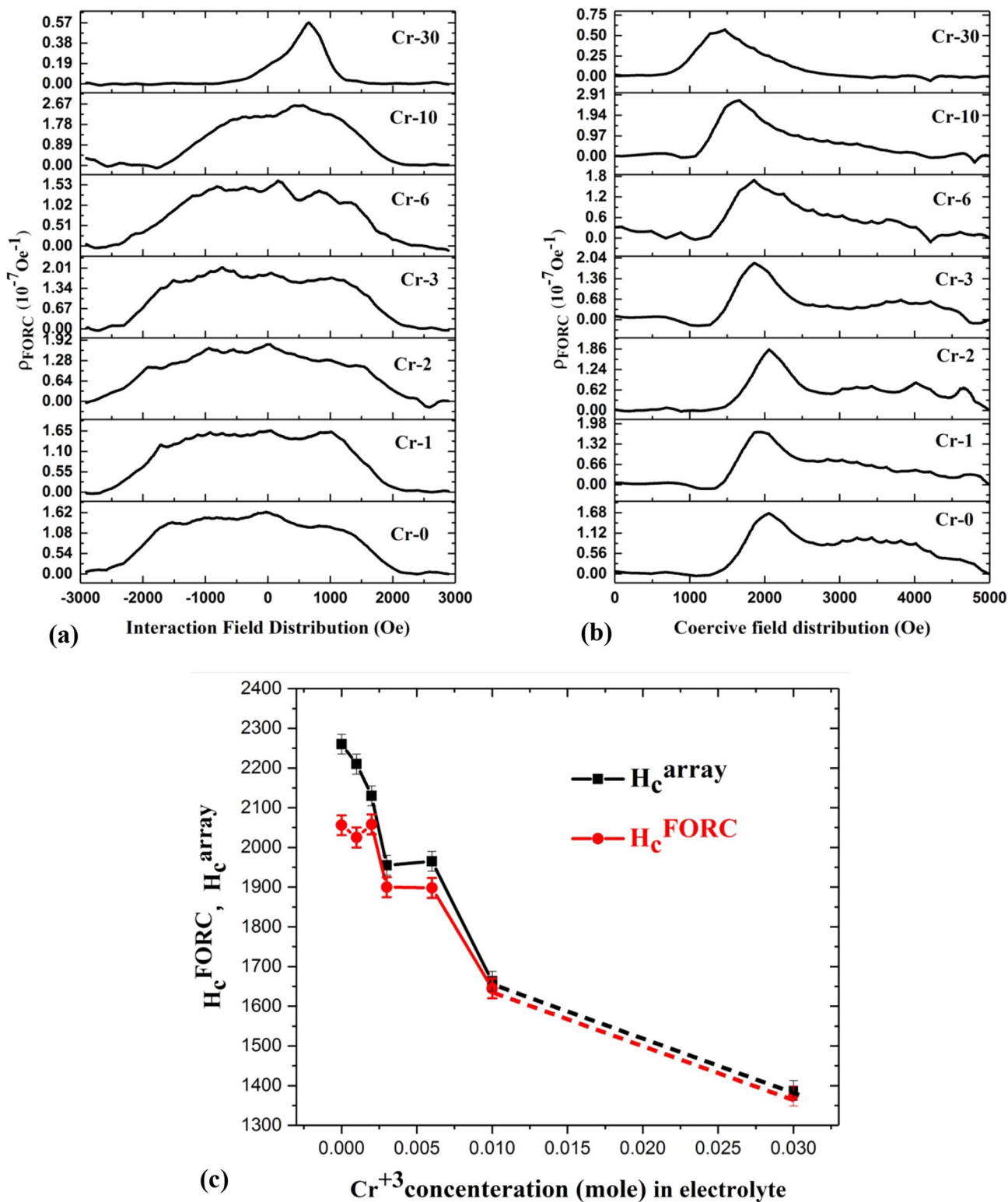
(c)

Fig. 7 **a** The cross-sectional view of FORC diagrams; along the H_u axis, (**b**) along the H_C axis at $H_u = 0$ and (**c**) variation of H_C^{array} and H_C^{FORC} as a function of the Cr concentration
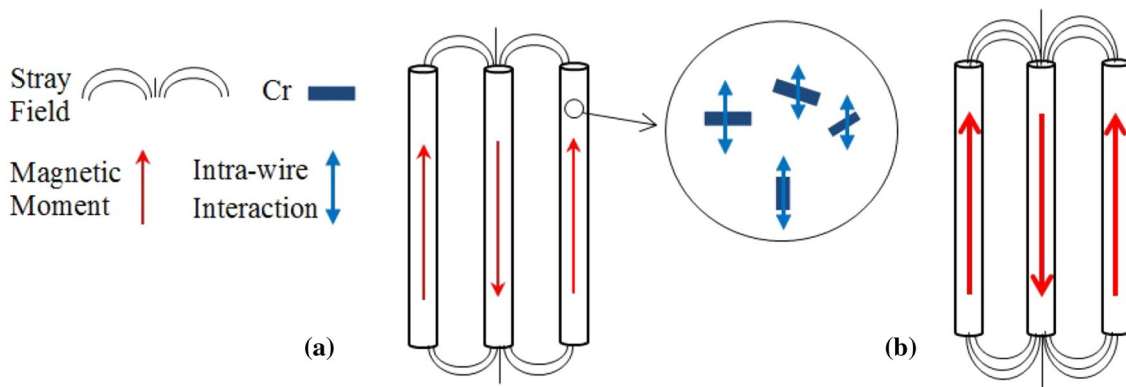
Fig. 8 The schematic illustration of inter-wire and intra-wire interaction for (FeCo)$_{1-x}$Cr$_x$ NWs, (**a**) with the Cr phase, and (**b**) without the Cr phase

References

1. V. Van Kerckhoven, L. Piraux, I. Huynen, Micromachines. **10**, 475 (2019)
2. T. Chen, P. Cavallotti, Appl. Phys. Lett. **41**, 205–207 (1982)
3. A.I. Martínez-Banderas, A. Aires, F.J. Teran, J.E. Perez, J.F. Cadenas, N. Alsharif, T. Ravasi, A.L. Cortajarena, J. Kosel, Sci. Rep. **6**, 35786 (2016)
4. A. Blondel, J.P. Meier, B. Doudin, J.P. Ansermet, Appl. Phys. Lett. **65**, 3019–3021 (1994)
5. L. Piraux, J.M. George, J.F. Despres, C. Leroy, E. Ferain, R. Legras, K. unadjela, A. Fert, Appl. Phys. Lett. (1994), 65, 2484–2486.
6. J.E. Wegrowe, D. Kelly, A. Franck, S.E. Gilbert, J.P. Ansermet, Phys. Phys. Rev. Lett. **82**, 3681 (1999)
7. A. H. Montazer, A. Ramazani, M. Almasi Kashi, and J. Zavašnik, Journal of Materials Chemistry C, 4 (45), 10664, (2016).
8. S.L. Viñas, R. Salikhov, C. Bran, E.M. Palmero, M. Vazquez, B. Arvan, X. Yao, P. Toson, J. Fidler, M. Spasova, U. Wiedwald, M. Farle, Nanotechnology. **26**(41), 415704 (2015)
9. Li. Wuxia, Y. Peng, G. A. Jones, T. H. Shen, and G. Hill, JOURNAL OF APPLIED PHYSICS. 97, 034308, (2005).
10. S. Kim, H. Yoon, H. Lee, S. Lee, Y. Jo, S. Lee, J. Choo, B. Kim, J. Mater. Chem. C **3**, 100 (2015)
11. D.B. Seley, D.A. Dissing, A.V. Sumant, R. Divan, S. Miller, O. Auciello, L.A. Lepak, E.A. Terrell, T.J. Shogren, D.A. Fahrner, J.P. Hamilton, M.P. Zach, ACS Appl. Mater. Interfaces. **3**, 925 (2011)
12. Z. Huang, Y. Zhang, F. Tang, Chem. Commun. **1**, 342 (2005)
13. F. Nasirpouri, Springer, cham. 187–259, (2017).
14. N.J. Gerein, J.A. Haber, J. Phys. Chem. B **109**(37), 17372–17385 (2005)
15. L. Trahey, C. R. Becker and A. M. Stacy Nano Letters., 7(8), 2535–2539, (2007).
16. K. Nielsch, F. Muller, A.-P. Li, U. Gosele, Adv. Mater. **12**(8), 582–586 (2000)
17. I. Panagiotopoulos, W. Fang, F. Ott, F. Boué, K. Ait-Atmane, J.Y. Piquemal, G. Viau, J. Appl. Phys. **114**, 143902 (2013)
18. R. Skomski, Y. Liu, J.E. Shield, G.C. Hadjipanayis, D.J. Sellmyer, J. Appl. Phys. **107**(9), 09A739 (2010)
19. A. Ramazani, M. Almasi Kashi, S. Kabiri and M. Zanguri, Journal of Crystal Growth, 327(1), 78–83, (2011).
20. K. Gandha, P. Tsai, G. Chaubey, N. Poudyal, K. Elkins, J. Cui, J.P. Liu, Nanotechnology **26**(7), 075601 (2015)
21. A. Ramazani, M. Almasi Kashi, S. Ghanbari, F. Eshaghi, Journal of Magnetism and Magnetic Materials, 324, 3193–3198, (2012).
22. C. Bran, E. Berganza, E. M.Palmero, J. A. Fernandez-Roldan, R. P.Del Real, L. Aballe, M. Foerster, A. Asenjo, A. Fraile Rodriguez, M. Vazquez, Journal of Materials Chemistry C, 4, 978–984, (2016).
23. B. Rodríguez-González, C. Bran, T. Warnatz, J. Rivas, M. Vazquez, J. Appl. Phys. **115**, 133904 (2014)
24. L. A. Rodríguez, C. Bran, D. Reyes, E. Berganza, M. V_azquez, C.Gatel, E. Snoeck, Asenjo, A. ACS nano, 10, 9669–9678, (2016).
25. E. Berganza, C. Bran, M. Jaafar, M. Vázquez, A. Asenjo, ACS Nano **10**, 6 (2016)
26. R. Sharif, S. Shamaila, M. Ma, L.D. Yao, R.C. Yu, X.F. Han, Yong Wang, M. Khaleeq-ur-Rahman, Journal of Magnetism and Magnetic Materials, 320 1512–1516, (2008).
27. R.L. Wang, S.L. Tang, Y.G. Shi, X.L. Fei, B. Nie, Y.W. Du, J. APP. Phys. **103**(7), 07D507 (2008)
28. S. Samanifar, M. Almasi Kashia, A. Ramazania, Physica. C. 548, 72–74, (2018).
29. F. Noori, A. Ramazani, M.A. Kashi, J. Alloy. Compd. **756**, 193–201 (2018)
30. M. Almasi-Kashi, A. Ramazani, E. Golafshan, M. Arefpour, E. Jafari-Khamse, Phys. B **429**, 46–51 (2013)
31. C. Bran, Yu.P. Ivanov, J. Garcia, R.P. del Real, V.M. Prida, O. Chubykalo-Fesenko, M. Vazquez, J. Appl. Phys. **114**, 043908 (2013)
32. E.M. Palmero, R. Salikhov, U. Wiedwald, C. Bran, M. Spasova, M. Vázquez, M. Farle, Nanotechnology. **27**(36), 365704 (2016)
33. D.H. Qin, Y. Peng, L. Cao, H.L. Li, Chem. Phys. Lett. **374**, 661–666 (2003)
34. Ch. Huang, P. Wang, W. Guan, S. Yang, L. Gao, L. Wang, X. Song, R. Murakami, Mater. Lett. **64**, 2465 (2010)
35. C.R. Pike, A.P. Roberts, K.L. Verosub, Geophys. J. Int. **145**, 721–730 (2001)
36. A.P. Roberts, D. Heslop, X. Zhao, C.R. Pike, Rev. Geophys. **52**, 557–602 (2014)
37. A.P. Roberts, C.R. Pike, K.L. Verosub, J. Appl. Phys. **85**(9), 6660 (1999)
38. G. Sharma, M.V. Pishko, C.A. Grimes, J Mater Sci. **42**, 4738–4744 (2007)
39. H. Schlörb, V. Haehnel, M.S. Khatri, A. Srivastav, A. Kumar, L. Schultz, S. Fähler, Phys. Status Solidi B. **247**(10), 2364–2379 (2010)

40. R. Gupta, R. Ansari, A. Khandelwal, J. Fassbender, A. Gupta, Nucl. Instruments Methods Phys. Res. B **266**(8), 1407–1410 (2008)

41. A. Ramazani, M. Almasi-Kashi, E. Golafshan, M. Arefpour, J. Cryst. Growth. **402**, 42–47 (2014)

42. D. Salazar-Aravena, J.L. Palma, J. Escrig, Materials Res. Express. **1**, 026112 (2014)

43. O. Albrecht, R. Zierold, S. Allende, J. Escrig, C. Patzig, B. Rauschenbach, K. Nielsch, D. Gorlitz, J. Appl. Phys. **109**, 093910 (2011)

44. P. Ivanov, M. Vazquez, O. Chubykalo-Fesenko, J. Phys. D: Appl. Phys. **46**, 485001 (2013)

45. N. Bajales, M. S. Viqueira, L. A. Silvia E. Urreta and Paula G., IEEE Trans. Magn. 49 8 (2013): 4610–4613.

46. J. Escrig, J. Bachmann, J. Jing, M. Daub, D. Altbir, K. Nielsch, Phys. Rev. B. **77**, 214421 (2008)

47. L.G. Vivas, M. Vazquez, J. Escrig, S. Allende, D. Altbir, D.C. Leitao, J.P. Araujo, Phys. Rev. B. **85**, 035439 (2012)

48. C.-I. Dobrota, A. Stancu, What does a first-order reversal curve diagram really mean? A study case: array of ferromagnetic nanowires. J. Appl. Phys. **113**, 043928 (2013)

49. F. Beron, L.-P. Carignan, D. Menard, A. Yelon, IEEE Trans. Magn. **44**, 11 (2008)

50. S. Alikhanzadeh-Arani, M. Almasi-Kashi, A. Ramazani, Curr. Appl. Phys. **13**, 664–669 (2013)

51. M. Ciureanu, F. Béron, P. Ciureanu, R.W. Cochrane, D. Menard, A. Sklyuyev, A. Yelon, J. Nanosci. Nanotechnol. **8**, 5725 (2008)

52. F. Beron, L. Clime, M. Ciureanu, D. Menard, R.W. Cochrane, A. Yelon, J. Nanosci. Nanotechnol. **8**, 2944–2954 (2008)